Dissipative Particle Dynamics Simulation of Ultrasound Propagation through Liquid Water

Petra Papež and Matej Praprotnik*

Read Online

ACCESS | Metrics & More | Article Recommendations | Supporting Information

ABSTRACT: Ultrasound is widely used as a noninvasive method in therapeutic and diagnostic applications. These can be further optimized by computational approaches, as they allow for controlled testing and rational optimization of the ultrasound parameters, such as frequency and amplitude. Usually, continuum numerical methods are used to simulate ultrasound propagating through different tissue types. In contrast, ultrasound simulations using particle description are less common, as the implementation is challenging. In this work, a dissipative particle dynamics model is used to perform ultrasound simulations in liquid water. The effects of frequency and thermostat parameters are studied and discussed. We show that frequency and thermostat parameters affect not only the attenuation but also the computed speed of sound. The present study paves the way for development and optimization of a virtual ultrasound machine for large-scale biomolecular simulations.
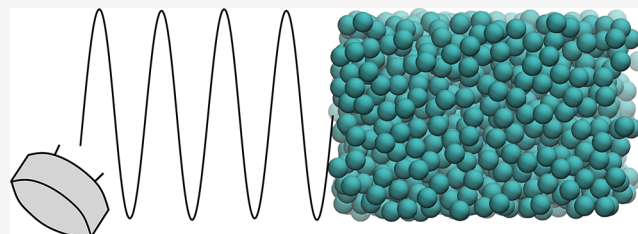
1. INTRODUCTION

Ultrasound consists of mechanical pressure waves, which can propagate through various media with frequencies above the upper limit of (average) human hearing, that is, above 20 kHz.[1−4] Unlike light, which is scattered roughly within 1 mm of tissue, ultrasound easily penetrates centimeters deep while maintaining spatial and temporal coherence.[2,5] For this reason, ultrasound is used in many medical applications. Nonetheless, ultrasound is also used in, for example, nanotechnology, sonochemistry,[6,7] food processing, industrial processes (e.g., welding), and nondestructive material investigation.[8,9] In medical applications, it is commonly used as a safe and noninvasive diagnostic (imaging) tool to diagnose many types of cancers, such as breast, stomach, and thyroid. Additionally, it is employed in therapeutic applications in cases of joint inflammation, rheumatoid arthritis, mechanical tissue disruption, kidney stone comminution, bone healing, and as an alternative treatment to the surgical resection of tumors.[10−15]

Due to its applicability, there is also a need for simulation methods that provide an insight into the phenomena that occur during ultrasound treatment or tissue imaging, and thus open the door to clinical applications. In most methods the assumption of isotropic, nondissipative, and homogeneous medium is made. However, these assumptions are typically oversimplistic and the computational cost is too high.[16−19] To this end, computationally more efficient methods incorporating heterogeneous tissue properties have also been proposed.[18,20−26]

Moving away from diagnostic ultrasound simulations, sound waves are simulated using classical mesh-based numerical methods, for example, the boundary element method (BEM),[27] the finite element method (FEM),[28,29] and their modifications.[30,31] On the other hand, also meshless methods are used, for example, the method of fundamental solutions (MFS),[32] the multiple-scale reproducing kernel particle method (RKPM),[33] and the element free Galerkin method (EFG).[34] In addition, the smoothed particle hydrodynamics method (SPH) has proven to be a promising particle-based method for sound simulations. It is able to accurately model the sound propagation, and the effects of sound frequency, maximum sound pressure amplitude, and particle spacing on the numerical error and time consumption were studied by Zhang et al.[35,36] Another contribution to simulations of ultrasound waves using a particle-based description[37] was made by De Fabritiis et al.[38,39] They proposed a coupled multiscale model, that is, hybrid molecular dynamics (MD). In the hybrid MD, the mesoscopic description of a fluid flow, based on the equations of fluctuating hydrodynamics (FH), is coupled with the molecular description of particles. By successfully coupling FH and classical MD, they have overcome the limitations of already existing hybrid descriptions of liquids that were limited to the coarse-grained (CG) descriptions based on the Lennard-Jones particles. Using the proposed hybrid MD method, they simulated sound waves,
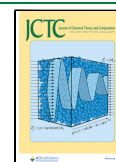
generated as the Gaussian density perturbation of the equilibrium state, in bulk water reflected by a lipid monolayer. Furthermore, Korotkin et al.[40] suggested a new method, that is, a hybrid MD/FH method, based on the two-phase flow analogy. The method smoothly combines the atomistic (AT) description in the MD zone with the Landau-Lifshitz fluctuating hydrodynamics (LL-FH) representation in the rest of the system. The simulation domain is divided into cells in all three directions, where the pure MD zone in the center of the simulation domain is surrounded by two Landau-Lifshitz domains. The boundary condition of the sound wave is introduced by adding the analytical source terms to the governing LL-FH equations for cells at the beginning of the simulation domain. The analytical source terms correspond to the time derivatives of the density and velocity of the incoming sound wave of small amplitude propagating over the prescribed constant mean flow field of the LL-FH solution. In a consecutive work, Hu et al.[41] extended the already existing hybrid MD/FH method[40] with the scale-bridging adaptive resolution scheme (AdResS). Additionally, Korotkin and Karabasov[42] developed the generalized LL-FH (GLL-FH) as the extension of the classical continuum LL-FH model in statistical mechanics. In the GLL-FH equations, compared to the classical LL-FH method, some additional time dependent solution variables are introduced, which describe the difference between the locally averaged fields, obtained by the MD, and the solution of continuum hydrodynamics.

In this work, we employ the mesoscopic dissipative particle dynamics (DPD) water model to perform the particle-based ultrasound simulations in the THz frequency range. To the best of our knowledge, there is no study available to examine the effects of ultrasound frequency, amplitude, and thermostat parameters on the propagation of ultrasound waves using the DPD model. Furthermore, ultrasound waves can be in general considered either as adiabatic or isothermal. In gases, low frequency sound waves are typically adiabatic, while the high frequency ones are isothermal.[43,44] However, in water, it is not a priori clear which classification is more appropriate for ultrasound propagation in the THz frequency range. We aim to clarify this issue by conducting our simulations. Finally, we will also test the propagation of ultrasound waves through water, described by the simple point charge (SPC) model,[45] using AdResS.

2. THEORETICAL BACKGROUND AND METHODOLOGY

2.1. Ultrasound. The dynamics of a viscous fluid is governed by the Navier−Stokes equation:

$$\rho\left[\frac{\partial \mathbf{v}}{\partial t} + (\mathbf{v}\cdot\nabla)\mathbf{v}\right] = -\nabla p + \eta\Delta\mathbf{v} + \left(\zeta + \frac{1}{3}\eta\right)\nabla\nabla\cdot\mathbf{v} \tag{1}$$

where ρ stands for the fluid density, p is for pressure, t is for time, and $\mathbf{v}$ represents the fluid velocity. Coefficients ζ and η are positive, and represent the second and dynamic viscosity, respectively. For the incompressible fluid flow, the last term in the Navier−Stokes equation is omitted.[46] If we further neglect the energy-dissipating second term on the right side in the Navier−Stokes equation, assume small oscillations, and consider the continuity equation, we obtain the wave equation for the velocity potential ϕ

$$\frac{\partial^2\phi}{\partial t^2} = c^2\Delta\phi \tag{2}$$

where $\mathbf{v} = \nabla\phi$. In the wave equation, c stands for the velocity of sound and is given by $c^2 = (\partial p/\partial\rho)$, either at constant entropy s or at constant temperature T. For instance, considering the monochromatic traveling plane wave, propagated in the positive direction of the x-axis, and introducing the wave vector $\mathbf{k}$ as $\mathbf{k} = (\omega/c)\mathbf{n} = (2\pi/\lambda)\mathbf{n}$, where $\mathbf{n}$ denotes a unit vector in the direction of the propagation of the sound wave and λ denotes the wavelength of the propagated sound wave, the solution of eq 2 is

$$\phi = \mathrm{Re}\left\{A \exp\left[-i\omega\left(t - \frac{x}{c}\right)\right]\right\} = \mathrm{Re}\{A \exp[i(\mathbf{k}\cdot\mathbf{r} - \omega t)]\} \tag{3}$$

where $A = ae^{i\varphi}$ represents the complex amplitude, $\mathbf{r}$ is the position vector, and Re stands for the real part. Parameters ω, a, and φ are the frequency of the wave, amplitude, and phase shift, respectively.

The propagation of any sound wave through a medium is governed by the wave equation. In this work, we simulate ultrasound waves and compare the obtained signals with the solutions corresponding to eq 3. Ultrasound consists of mechanical pressure waves ($p = -\rho\partial\phi/\partial t$), which can propagate through media with frequencies above the audible threshold of 20 kHz. From the experimental point of view, the most commonly varied ultrasound parameters are frequency, intensity, applied acoustic pressure, mechanical index (defined as the peak negative pressure divided by the square root of center frequency), and duration of the exposure to the ultrasound.[1,47−50] Accordingly, the parameters of interest in our study are the frequency and amplitude of the oscillatory part of the simulated ultrasound waves.

As already mentioned, sound waves can be isothermal or adiabatic.[43,44] Each medium has a frequency associated with thermal conduction (TC), expressed as $\omega_{TC} = \rho c_p c^2/\kappa_{TC} = 2\pi\nu_{TC}$, where c_p and κ_{TC} stand for the heat capacity at constant pressure and coefficient of thermal conductivity, respectively. $\omega_{TC}/2\pi$ for water is of the order of 2 THz.[44] At very high frequencies, that is, if $\omega \gg \omega_{TC}$, the process of sound propagation can be considered as isothermal, while the adiabatic approximation is better at lower frequencies, that is, if $\omega \ll \omega_{TC}$.[43,44,51] However, for water it is expected that there is a negligible difference between the isothermal or adiabatic approximation, as $\Delta\kappa/\kappa \sim 10^{-4}$. Besides, at THz frequencies corresponding wavelengths are comparable to the mean free path of water molecules and we approach the limit of validity of the thermodynamics.

2.2. Dissipative Particle Dynamics (DPD). We simulate ultrasound on a mesoscopic level using a particle-based DPD method. It is particularly suitable for simulating liquids and soft matter since its linear momentum conserving equations of motion recover the Navier−Stokes equations in the continuum limit (FH).[52−54] The CG nature of a DPD model enables simulations on larger time and length scales. The underlying idea of DPD is that many important properties of soft matter are determined by the collective properties of clusters of molecules rather by individual molecules.[55−57] For instance, the DPD method has been applied to colloidal suspensions, multiphase flows, biological systems,[58−60] and vesicle formation.[61] The DPD equations of motion are

$$\dot{\mathbf{r}}_i = \frac{\mathbf{p}_i}{m_i} \tag{4}$$

and

$$\dot{\mathbf{p}}_i = \mathbf{F}_i^C + \mathbf{F}_i^D + \mathbf{F}_i^R \tag{5}$$

$\mathbf{F}_i^C$, $\mathbf{F}_i^D$, and $\mathbf{F}_i^R$ stand for the conservative, dissipative, and random force on the ith particle, respectively. They can be split into particle pair forces:

$$\mathbf{F}_i^C = \sum_{j \neq i} \mathbf{F}_{ij}^C \tag{6}$$

$$\mathbf{F}_i^D = \sum_{j \neq i} \mathbf{F}_{ij}^D \tag{7}$$

and

$$\mathbf{F}_i^R = \sum_{j \neq i} \mathbf{F}_{ij}^R \tag{8}$$

The conservative force is

$$\mathbf{F}_{ij}^C = a_{ij}\left(1 - \frac{r_{ij}}{r_c}\right)\mathbf{e}_{ij} \tag{9}$$

where $\mathbf{r}_{ij} = \mathbf{r}_i - \mathbf{r}_j$, $r_{ij} = |\mathbf{r}_{ij}|$, $\mathbf{e}_{ij} = \mathbf{r}_{ij}/r_{ij}$, and $\mathbf{r}_i$, $\mathbf{r}_j$ are the position vectors of particle i and j, respectively. Parameter a_{ij} stands for the repulsion strength. This force becomes zero for $r_{ij} \geq r_c$, where r_c stands for the cutoff radius. The dissipative force is

$$\mathbf{F}_{ij}^D = -\gamma_\| \omega^D(r_{ij})(\mathbf{v}_{ij} \cdot \mathbf{e}_{ij})\mathbf{e}_{ij} \tag{10}$$

and the random force is

$$\mathbf{F}_{ij}^R = \sigma_\| \omega^R(r_{ij})\mathbf{e}_{ij}\Theta_{ij} \tag{11}$$

where the relative velocity $\mathbf{v}_{ij} = \mathbf{v}_i - \mathbf{v}_j$ between two particles i and j is introduced. $\gamma_\|$ is the friction constant and $\sigma_\|$ is the noise strength. $\omega^R(r_{ij})$, and $\omega^D(r_{ij})$ are the r-dependent weight functions. They are related by the fluctuation−dissipation theorem:

$$\omega^D(r) = [\omega^R(r)]^2 \tag{12}$$

$$(\sigma_\|)^2 = 2\gamma_\| k_B T \tag{13}$$

and defined as

$$\omega^R(r) = \omega^D(r) = \begin{cases} 1 & \text{when } r < r_c \\ 0 & \text{when } r \geq r_c \end{cases} \tag{14}$$

Θ_{ij} in eq 11 is Gaussian white noise, symmetric in the particle indices ($\Theta_{ij} = \Theta_{ji}$), with zero mean $\langle\Theta_{ij}(t)\rangle$ and unit variance $\langle\Theta_{ij}(t)\Theta_{kl}(t')\rangle = (\delta_{ik}\delta_{jl} + \delta_{il}\delta_{jk})\delta(t - t')$, where $\langle.\rangle$ denotes the thermal average. In addition, the above DPD equations conserve the linear momentum and correctly reproduce the hydrodynamic interactions in the system.[62,63] Together, dissipative and random forces act as a thermostat.[64,65] We distinguish between two DPD thermostats, that is, the standard one (presented above) that acts on the relative velocities along the interatomic axis and the transverse dissipative particle dynamics (TDPD) thermostat that acts in perpendicular directions and enables viscosity tuning.[65] In the TDPD thermostat, eq 10 is rewritten into

$$\mathbf{F}_{ij}^D = -\omega^D(r_{ij})[\gamma_\|(\mathbf{e}_{ij} \otimes \mathbf{e}_{ij}) + \gamma_\perp(\mathrm{I} - \mathbf{e}_{ij} \otimes \mathbf{e}_{ij})]\mathbf{v}_{ij} \tag{15}$$

and eq 11 is rewritten into

$$\mathbf{F}_{ij}^R = \omega^R(r_{ij})[\sigma_\|(\mathbf{e}_{ij} \otimes \mathbf{e}_{ij}) + \sigma_\perp(\mathrm{I} - \mathbf{e}_{ij} \otimes \mathbf{e}_{ij})]\Theta_{ij} \tag{16}$$

where Θ_{ij} is the noise vector, defined as $\langle\Theta_{ij}(t) \otimes \Theta_{kl}(t')\rangle = \mathrm{I}(\delta_{ik}\delta_{jl} - \delta_{il}\delta_{jk})\delta(t - t')$. The noise vector is antisymmetric in particles indices ($\Theta_{ij} = -\Theta_{ji}$). Apart from relations in eqs 12 and 13, the relation $(\sigma_\perp)^2 = 2\gamma_\perp k_B T$ needs to be fulfilled.[65]

2.3. Open Boundary Molecular Dynamics (OBMD). To simulate ultrasound waves we need to open the molecular system so it can exchange mass, momentum, and energy with its surroundings. To achieve this goal, we resort to the OBMD.[66−70] In OBMD, the simulation box is opened in one direction (or more), while the periodic boundary conditions are imposed in the remaining ones. The box is divided into three regions, where the central region, named the region of interest (ROI), is surrounded by two buffer regions. The latter act as particle reservoirs from which molecules are deleted and inserted into the system. The number of particles (or density) in the buffers is maintained by the feedback algorithm. The feedback algorithm is defined as $\Delta N_B = (\delta t/\tau_B)(\langle N_B\rangle - N_B)$, where $\langle N_B\rangle$ represents the desired number of molecules inside the buffer and N_B stands for the current number of molecules inside the buffer. Parameter τ_B denotes the characteristic relaxation time of the buffers ($\approx O(100\delta t)$). When $\Delta N_B < 0$, molecules need to be deleted from the system. Conversely, when $\Delta N_B > 0$, new molecules need to be inserted into the system. The insertion of new DPD particles is carried out by the iterative algorithm named USHER, which is a Newton-Raphson-like search method on the potential energy surface.[71,72] The total linear momentum in the OBMD is conserved, which directly follows from the Navier−Stokes equation given by eq 1. The latter can be reformulated into a linear momentum conservation law as $\partial(\rho\,\mathbf{v})/\partial t = -\nabla\cdot\mathbf{J}^P$, where $\mathbf{J}^P$ stands for the momentum flux tensor, defined as $\mathbf{J}^P = \rho\mathbf{u} \otimes \mathbf{u} + \Pi + \tilde{\Pi}$. Here, Π and $\tilde{\Pi}$ are the mean and fluctuating contributions to the pressure tensor, respectively. The mean pressure is usually defined as $\Pi = (p + \pi)\mathrm{I} + \Pi^S$, where p stands for the pressure of the system (usually obtained from the equation of state), I represents the identity matrix, π represents the isotropic stress ($\pi = -\zeta\nabla\cdot\mathbf{u}$), and Π^S is the traceless symmetric tensor, expressed as $\Pi^S_{\alpha\beta} = -\eta(\partial_\alpha u_\beta + \partial_\beta u_\alpha - 2\partial_\gamma u_\gamma \delta_{\alpha\beta}/D)$. Here, D represents the spatial dimension.[38,73]

OBMD imposes the external boundary conditions through buffers onto the ROI by an additional external force $\mathbf{f}_i^{ext}$ that is applied only to the particles in the buffer regions; that is, $\mathbf{f}_i^{ext} = 0$ outside the buffer region. Boundary conditions are defined by the normal component of the energy flux, that is, the rate of energy transfer through a surface, as $J_e = \mathbf{J}_e\cdot\mathbf{n}$, where $\mathbf{J}_e$ represents the energy flux vector and $\mathbf{n}$ is the unit vector normal to the interface between buffer and ROI (pointing toward the center of ROI), and by the momentum flux $\mathbf{J}^P\cdot\mathbf{n}$, where $\mathbf{J}^P$ stands for the already defined momentum flux tensor. To determine external forces, the amount of momentum and energy created by these forces over one time step dt needs to be considered and the result equated to the desired amount of momentum and heat that needs to be added to or extracted from the system. The momentum balance of A, that is, the area of the interface between buffer and ROI, is

$$\mathbf{J}^P \cdot \mathbf{n}A\,\mathrm{d}t = \sum_{i \in B} \mathbf{f}_i^{ext}\,\mathrm{d}t + \sum_{i'} \Delta(m_{i'}\mathbf{v}_{i'}) \tag{17}$$

and the energy balance is

(a) Momentum-flux-exchanging *setup 1*.

(b) Momentum-flux-exchanging *setup 2*.
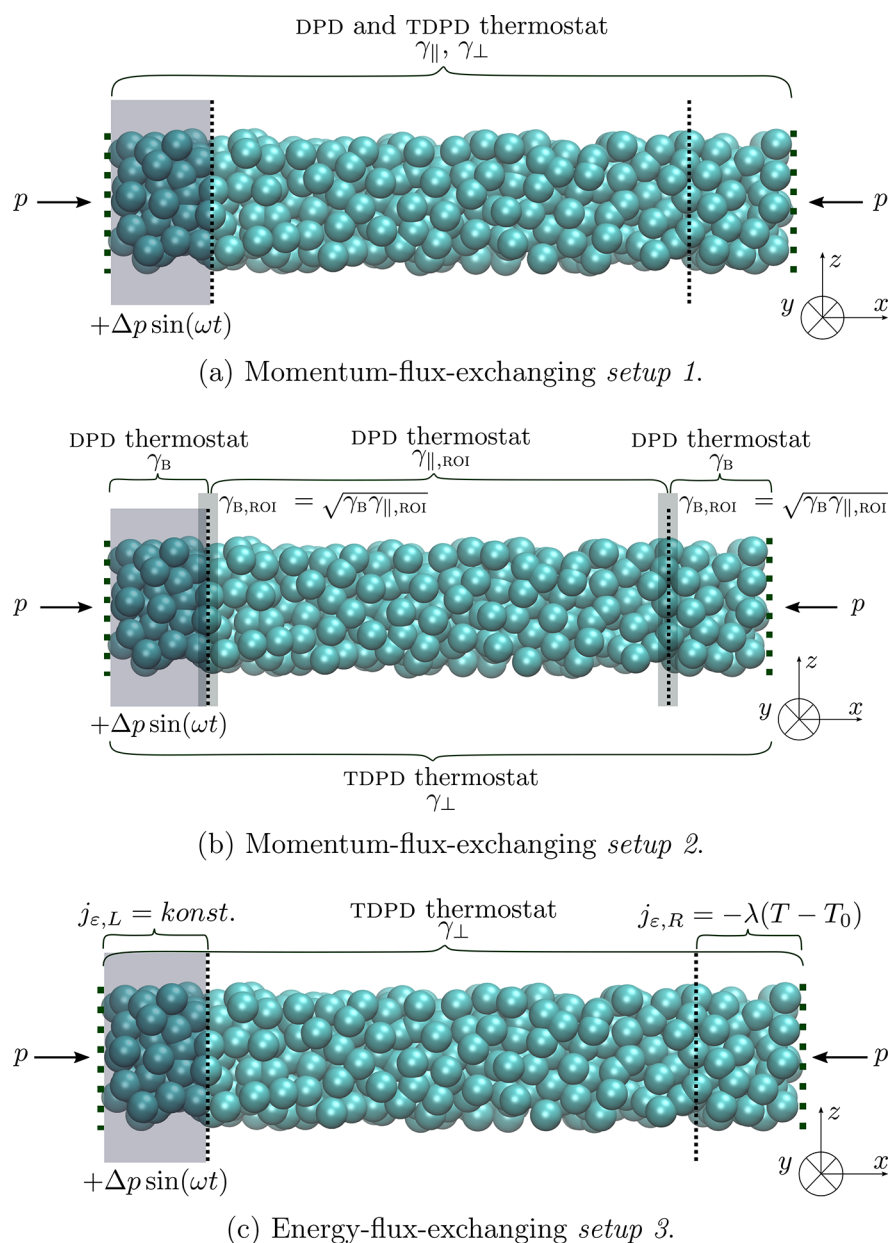

(c) Energy-flux-exchanging *setup 3*.

Figure 1. Schematic representations of the *setups* used in the OBMD to simulate the propagation of an ultrasound wave through a DPD water.

$$J_e A\, dt = \sum_{i \in B} \mathbf{f}_i^{\text{ext}} \cdot \mathbf{v}_i\, dt + \sum_{i'} \Delta \epsilon_{i'} \tag{18}$$

In eqs 17 and 18, i' runs over all particles that have been inserted into or deleted from the system in the last time step dt, while i runs over all particles that are within buffer regions. The momentum change $\Delta(m_i \mathbf{v}_{i'}) = m_i \mathbf{v}_{i'}$ if the particle is inserted into the system and $\Delta(m_i \mathbf{v}_{i'}) = -m_i \mathbf{v}_{i'}$ if the particle is deleted from the system. Similarly, this applies to the energy change $\Delta \epsilon_{i'}$. The balance of eqs 17 and 18 ensures that the total momentum and energy are conserved. Boundary conditions impose the exact momentum and energy flux to the whole system (i.e., buffers + ROI). Since buffer has some mass and heat capacity, the momentum transfer across the interface between buffer and ROI is not instantaneously equal to the amount prescribed by the momentum and energy flux defined in eqs 17 and 18. However, in real applications this effect is usually negligible.[66,68]

To separate momentum from heat generation the external force $\mathbf{f}_i^{\text{ext}}$ is divided into two parts:

$$\mathbf{f}_i^{\text{ext}} = G(\mathbf{r}_i \cdot \mathbf{n})\mathbf{F}^{\text{ext}} + \tilde{\mathbf{f}}_i^{\text{ext}} \tag{19}$$

where $\mathbf{F}^{\text{ext}}$ and $\tilde{\mathbf{f}}_i^{\text{ext}}$ represent momentum and energy contributions, respectively. The force $\mathbf{F}^{\text{ext}} = \sum_{i \in B} \mathbf{f}_i^{\text{ext}}$ is distributed among particles in the buffers, where $G(\mathbf{r}_i \cdot \mathbf{n})$ represents the distributing tensor:

$$G(\mathbf{r}_i \cdot \mathbf{n}) = g(\mathbf{r}_i \cdot \mathbf{n}) / \sum_{i \in B} g(\mathbf{r}_i \cdot \mathbf{n})\mathbf{n} \otimes \mathbf{n}$$

Note that $\mathbf{r}_i \cdot \mathbf{n}$ is the distance from the interface in the x-direction. Using eq 17,

$$\mathbf{F}^{\text{ext}} = A\left(\mathbf{J}^P \cdot \mathbf{n} - \frac{\sum_{i'} \Delta(m_i \mathbf{v}_{i'})}{A\, dt}\right) \tag{20}$$
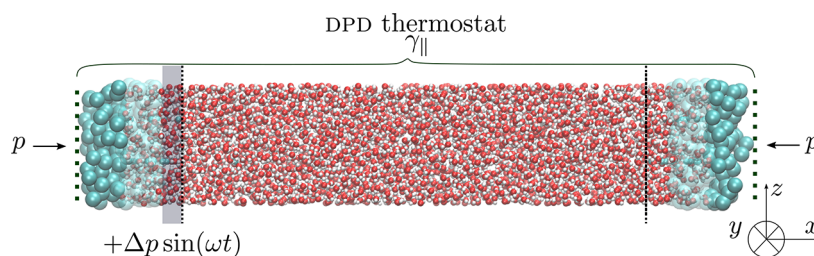
Figure 2. Schematic representation of the momentum-flux-exchanging *setup* used in the OBMD to simulate the propagation of an ultrasound wave through the high resolution water described by the SPC water model.

The force $\tilde{\mathbf{f}}_i^{\text{ext}}$ that gives no net momentum input, that is, $\sum_{i \in B} \tilde{\mathbf{f}}_i^{\text{ext}} = 0$, is

$$\tilde{\mathbf{f}}_i^{\text{ext}} = \frac{A\mathbf{v}_i'}{\sum_{i \in B} \mathbf{v}_i'^2}\left[\left(J_e - \frac{\sum_{i'}\Delta\epsilon_{i'}}{A\,\mathrm{d}t}\right) - \left(\mathbf{J}^P\cdot\mathbf{n} - \frac{\sum_{i'}\Delta(m_i\mathbf{v}_i)}{A\,\mathrm{d}t}\right)\cdot\langle\mathbf{v}\rangle\right] \tag{21}$$

where velocity $\mathbf{v}_i' = \mathbf{v}_i - \langle\mathbf{v}\rangle$ and average velocity $\langle\mathbf{v}\rangle = \sum_{i \in B}\mathbf{v}_i/N_B$.[66,74]

In this study, J_e is fixed or controlled via $J_e = -\lambda(T - T_0)$,[66] where T stands for the current buffer temperature, T_0 is its desired temperature, and λ represents the adjustable relaxation parameter. Note that the external boundary conditions are introduced into the system without modification of Newton's equations of motion for particles in the bulk.[68,75]

Setup 1

momentum-flux exchange	yes
energy-flux exchange	no
DPD thermostat	yes, fixed thermostat parameters
TDPD thermostat	yes
governing equations	eqs 5, 15, 16, 17, 20

Setup 2

momentum-flux exchange	yes
energy-flux exchange	no
DPD thermostat	yes, varied thermostat parameters
TDPD thermostat	yes
governing equations	eqs 5, 15, 16, 17, 20

Setup 3

momentum-flux exchange	no
energy-flux exchange	yes
DPD thermostat	no
TDPD thermostat	yes
governing equations	eqs 5, 15, 16, 17, 18, 20, 21

Three different *setups* are used to simulate ultrasound. *Setups 1* and *2* are momentum-flux-exchanging, while *setup 3* is energy-flux-exchanging. The governing equations for the

implementation of both *setups 1* and *2* are eqs 17 and 20. Since the DPD thermostat is used in both *setups*, also eqs 5, 15, and 16 are valid. In momentum-flux-exchanging *setup 1*, the DPD thermostat acts on all particles within the simulation domain, that is, buffer + ROI, and the friction coefficient in the parallel direction (i.e., $\gamma_\parallel$) has a constant value. To check the effect of $\gamma_\parallel$ on the attenuation of ultrasound waves, different $\gamma_\parallel$ are inspected for the momentum-flux-exchanging *setup 2*. The value of $\gamma_\parallel$ depends on the position of a given particle. It is constant for particles inside buffers (i.e., $\gamma_{\parallel,\mathrm{B}}$) and it varies for particles within ROI (i.e., $0.0M_{\mathrm{DPD}}/\tau_{\mathrm{DPD}} \leq \gamma_{\parallel,\mathrm{ROI}} \leq 4.0M_{\mathrm{DPD}}/\tau_{\mathrm{DPD}}$). If one particle is located in the buffer region and other in the ROI, it is calculated as the geometric mean of both $\gamma_{\parallel,\mathrm{B}}$ and $\gamma_{\parallel,\mathrm{ROI}}$. When the energy-flux-exchanging *setup 3* is implemented, only energy transfer contribution is considered, in which the DPD thermostat is switched off and only the TDPD thermostat is applied. Therefore, the governing equations for the implementation of this *setup* are eqs 5, 15, 16, 17, 18, 20, and 21. In all *setups*, the ROI is located in the center of the simulation box, that is, between two buffer regions (in Figure 1 depicted with black dotted lines).

The external boundary condition of a constant normal load ($p = P^{\text{ext}}$) is applied onto the ROI through both buffer ends to keep the liquid inside the simulation domain. The ultrasound wave is generated by adding the oscillating pressure contribution $\Delta p \sin(\omega t)$ to one of the buffer ends (this region is indicated by a gray rectangle at the left side of the simulation domain in Figure 1). Correspondingly, the momentum flux tensor on the ultrasound wave generation (left) side is defined as $J_{ij}^P = (p + \Delta p \sin(\omega t))\delta_{ij}$, while the momentum flux tensor on the opposite side of the simulation domain is expressed as $J_{ij}^P = p\delta_{ij}$.

Setups 1 and *2* are expected to be suitable for studying isothermal systems, while *setup 3* is expected to be better suited for inspecting adiabatic systems. Performing OBMD simulations, we will test the presented *setups* to determine which one is more appropriate to perform simulations of ultrasound waves in the THz range.

To match the viscosity of a DPD water with the viscosity of the SPC water, we couple the TDPD thermostat with the standard DPD thermostat. In contrast to simulations using soft DPD particles, in all-atom simulations, the insertion of water molecules is rather difficult due to the possible overlap with the particles of molecules already present in the system. One approach to tackle this is to use a generalized USHER algorithm.[72] In addition to the vanilla USHER algorithm[71] described above, in the generalized scheme, insertion of a molecule at the prescribed potential energy is achieved not only by translation, but also by rotating the molecule around its center of mass. Another way is to follow a multiscale approach,[69,76,77] in which one uses CG-particle description to

insert molecules. In this approach, the buffer region consists of three parts of different resolutions, as depicted in Figure 2. The part adjacent to the ROI is described in the high (AT) description, while the low (CG) resolution particle description is used at the open ends of the simulation box. New CG molecules are inserted into the low resolution part of the buffer, where soft intermolecular interactions are acting between CG particles. Soft intermolecular interactions can be obtained, for example, by the iterative Boltzmann inversion method (IBI).[78,79] Inserted CG particles can freely diffuse from the low to the high resolution domain of the simulation box and acquire atomistic degrees of freedom. The bridging between different levels of description in the same simulation box is done by AdResS, as discussed next.

2.4. Adaptive Resolution Scheme (AdResS). AdResS[80−82] is a scheme that concurrently couples different levels of molecular description in the same simulation box. The latter is divided into three regions, AT, CG, and HY regions. The AT region is located in the center of the simulation box. In this region, molecules are described in high resolution. On the other hand, low resolution molecules are present in the CG regions, which are located at the ends of the simulation box. The smooth transition between the low and high resolution level of description (and *vice versa*) takes place in the HY region, which is located between the AT and CG regions. The total intermolecular force acting between two molecules α and β is

$$\mathbf{F}_{\alpha\beta} = w(\mathbf{r}_\alpha)w(\mathbf{r}_\beta)\mathbf{F}_{\alpha\beta}^{AT} + [1 - w(\mathbf{r}_\alpha)w(\mathbf{r}_\beta)]\mathbf{F}_{\alpha\beta}^{CG} \quad (22)$$

where

$$\mathbf{F}_{\alpha\beta}^{AT} = \sum_{i\alpha j\beta} \mathbf{F}_{i\alpha j\beta}^{AT} \quad (23)$$

and

$$\mathbf{F}_{i\alpha j\beta}^{AT} = -\frac{\partial U^{AT}}{\partial \mathbf{r}_{i\alpha j\beta}} \quad (24)$$

$\mathbf{F}_{\alpha\beta}^{AT}$ is the AT contribution to the intermolecular force and U^{AT} represents the intermolecular potential between AT particles. The CG contribution to the intermolecular force is

$$\mathbf{F}_{\alpha\beta}^{CG} = -\frac{\partial U^{CG}}{\partial \mathbf{R}_{\alpha\beta}} \quad (25)$$

where U^{CG} stands for the intermolecular potential between CG particles. The vector $\mathbf{r}_{i\alpha j\beta} = \mathbf{r}_{i\alpha} - \mathbf{r}_{j\beta}$ is the relative position vector of atoms i in molecule α and atoms j in molecule β. $\mathbf{R}_{\alpha\beta} = \mathbf{R}_\alpha - \mathbf{R}_\beta$ is the relative position vector of centers of mass of molecules α and β. w is the position dependent weighting function. For molecules within the AT region, ω is equal to 1, whereas for molecules within the CG region it is equal to 0. In the HY region, it changes its value from one to another. The total force between two molecules α and β obeys Newton's third law ($\mathbf{F}_{\alpha\beta} = -\mathbf{F}_{\beta\alpha}$) and like DPD conserves the linear momentum.[80,81] However, the force-based AdResS does not conserve energy, and the force defined in eq 22 is in general not conservative in the transition region. Consequently, to supply or remove the latent heat associated with the change of level of description, a locally acting thermostat is required, the forces of which are just added to the scheme.[82,83] Here, the DPD thermostat is used (see section 2.2).

3. COMPUTATIONAL DETAILS

3.1. DPD Details. For the mesoscopic DPD water model, we choose an 8-to-1 mapping scheme.[84] Therefore, the coarse-graining parameter N_m, representing the number of water molecules in one DPD particle, is 8. The mass of one DPD particle M_{DPD} corresponds to $m_i N_m$, where m_i stands for a mass of one water molecule. The DPD number density $\bar{\rho}$, defined as the number of beads contained in a cube of volume R_c^3, is set to 3. The physical length scale is set by $R_c = 3.107\sqrt[3]{\bar{\rho} N_m/\rho_w(T)}$, where $\rho_w(T)$ stands for the density of liquid water (in g/cm^3) at a temperature T. The unit of time is set by $\tau_{DPD} = R_c\sqrt{M_{DPD}/k_B T}$. The physical scale for force in a single-component system is set by the repulsion parameter $\bar{a}_{ij}$ and is usually defined by $\bar{a}_{ij} = (N_m \kappa_{exp}^{-1} - 1)/2\alpha\bar{\rho}$ (in units of $k_B T/R_c$). By adjusting the repulsion parameter, the experimental compressibility κ of the system is reproduced. Liquid water at room temperature has a compressibility of $\kappa_{exp}^{-1} \approx 16$. The friction coefficient in the parallel direction is set with $\gamma_\parallel = 4.5\sqrt{M_{DPD}k_B T}/R_c$.[55,84,85] Usually, the equations of motion are integrated using a modified velocity Verlet algorithm,[62] but in this work, the standard velocity Verlet algorithm is used and a time step of $0.001\tau_{DPD}$. The energy scale is given by $\varepsilon_{DPD} = k_B T$.

3.2. Atomistic Simulation Details. In OBMD simulations, atomistic SPC water molecules[86] are only present in the ROI, while low resolution particles representing one water molecule are present in the CG region. The choice of using the SPC water model was motivated by performing hybrid simulations, where for coupling to supramolecular water models (e.g., MARTINI and DPD) bundled water models formed by introducing half-harmonic bonds between atomistic SPC waters are employed.[84,87−89] We simulate the water system at ambient conditions, that is, at a temperature of 300 K and density 998 kg/m^3. The intermolecular interactions are described with the Lennard-Jones potential. The cutoff distance for the nonbonded interactions is 2.84σ, and they are capped at 0.54σ, 0.25σ, and 0.44σ for oxygen−oxygen, oxygen−hydrogen, and hydrogen−hydrogen interactions, respectively, where σ stands for the length scale. The cutoff distance for the DPD thermostat equals to the cutoff distance of the nonbonded interactions. The reaction field method is used for the electrostatic interactions beyond the cutoff. The dielectric permittivity is set to 1 and 80 for the inner and outer regions, respectively. The geometry of the water molecules is constrained using SETTLE.[90] Soft intermolecular interactions between CG particles are obtained by the IBI method.[78,79] The conservative force in the DPD equations of motion (see eq 5) is replaced by the force derived from the atomistic force field, where dissipative and random forces remain the same (application of the DPD thermostat[64,65]). The equations of motion are integrated using the velocity Verlet algorithm[91] and a time step of $0.0006\tau_{MD}$, where τ_{MD} represents a unit of time. Mass and energy scale is given by M_{MD} and ε_{MD}, respectively.

3.3. Computing Temperature Profile, Speed of Sound, and Attenuation Coefficient from Ultrasound Simulation. Simulations of length $500 \times t_0$ are performed, where t_0 stands for a time needed for one oscillation, and the last $400 \times t_0$ is used for the production run. In addition, to simulate ultrasound waves of different frequencies, we need to resort to different sizes of simulation boxes due to the reflection of ultrasound waves with lower frequency at the

Table 1. Computed Properties with Associated Standard Deviations and Parameters Used in Simulations of SPC and DPD Water, and Experimentally Determined Properties for Water at 25 °C

model	$\gamma_\parallel$	$\gamma_\perp$	η	c
SPC	0.049 $[M_{MD}/\tau_{MD}]$	0.0 $[M_{MD}/\tau_{MD}]$	17.60 ± 0.06 $[\varepsilon_{MD}\tau_{MD}/\sigma^3]$	7 ± 2 $[\sigma/\tau_{MD}]$
			0.940 ± 0.003 $[10^{-3}$ Pa s$]$	1487 ± 640 $[m/s]$
DPD	4.5 $[M_{DPD}/\tau_{DPD}]$	1.5 $[M_{DPD}/\tau_{DPD}]$	23.3 ± 0.3 $[\varepsilon_{DPD}\tau_{DPD}/R_c^3]$	11.4 ± 0.1 $[R_c/\tau_{DPD}]$
Experiment			0.890[100] $[10^{-3}$ Pa s$]$	1479[100] $[m/s]$

boundary between buffer and ROI. These spurious reflections can also be overcome by using nonreflecting boundary conditions.[92]

After every ultrasound simulation, the temperature profile through the simulation box is computed. Accordingly, the simulation box is divided into n_x bins in the direction of the ultrasound propagation (i.e., x-direction), where the number of bins depends on the size of the simulation box. The temperature in each bin is calculated by the equipartition theorem, followed by averaging over the simulation time.

To determine the speed of sound and attenuation coefficient, density signals over time are first calculated. To obtain density signals over time, the ROI is divided into $n_x \times n_y \times n_z$ cells in the x-, y-, and z-directions, where the number of cells depends on the size of the ROI. The density is calculated for each cell and space-averaged in the $y-z$ plane corresponding to the homogeneous directions. Additionally, the trajectory is divided into time intervals corresponding to t_0, followed by phase averaging. For each cell in the open direction (i.e., in the direction of the propagating ultrasound wave), the density signal over time t_0 is computed.

Afterward, for each cell (i.e., at different distances), the parameter k is computed using $\rho(x,t) = \rho_0 + \overline{\rho} \sin(\omega t - kx + \varphi)$, where ω, x, and φ are known input parameters. Quantity ρ_0 stands for the unattenuated amplitude of the propagating ultrasound wave, and $\overline{\rho}$ stands for the amplitude. The parameter k is at first free in order to determine the best value. The speed of sound is determined from the best fitting parameter k, which is used again in the above equation to determine $\overline{\rho}$ for each cell. The attenuation coefficient is finally calculated using $\overline{\rho}(x) = be^{-\alpha x}$.

4. RESULTS AND DISCUSSION

In water, ultrasound waves with the frequency in the MHz range travel the distance of several centimeters or even meters. In contrast, ultrasound waves in the THz range are absorbed on a very short distance.[38,51,66,74,93] Nevertheless, we focus here on simulations of ultrasound waves in the THz range because our future applications will be concerned with excitation of the low-frequency vibrational modes in biomolecules.[94−97]

We perform molecular simulations both in and out of thermodynamic equilibrium using the OBMD method. Since our primary interest is the propagation of ultrasound waves we first determine the equation of state (EOS) and calculate the speed of sound for the SPC and DPD water models from equilibrium simulations at different constant normal loads (i.e., different $p = P^{ext}$). We then determine the viscosity of simulated systems from simulations under shear flow at different strengths.[69] We present computed properties in Table 1 together with the experimentally obtained data. The computed viscosity of the SPC water model is close to the experimentally determined viscosity for water at 25 °C. For comparison, Smith et al.,[98] by performing equilibrium MD

simulations, and Song et al.,[99] by nonequilibrium MD, determined that the viscosity of the SPC water model is approximately 0.5 mPa s. The approximately two times higher viscosity is due to different thermostats used (Berendsen vs DPD) in these works. The speed of sound determined from the EOS of the SPC water corresponds to the experimentally determined speed of sound for water. The viscosity of the DPD water can be matched to the viscosity of the simulated SPC water by applying the TDPD thermostat in DPD simulations. Conveniently, a speed of sound computed from the EOS for the DPD water corresponds to the speed of sound for the SPC water.

As a representative set of ultrasound frequencies in the THz range, we choose six different frequencies which are further divided into low ($0.92\tau_{DPD}^{-1}$, $0.46\tau_{DPD}^{-1}$, $0.27\tau_{DPD}^{-1}$) and high ($2.76\tau_{DPD}^{-1}$, $2.15\tau_{DPD}^{-1}$, $1.84\tau_{DPD}^{-1}$). To investigate the ultrasound properties, that is, the attenuation and speed of sound, of the simulated ultrasound waves, we use three boxes of different dimensions, $30 \times 10 \times 10 R_c^3$, $130 \times 5 \times 5 R_c^3$, and $260 \times 5 \times 5 R_c^3$ in the x-, y-, and z-directions. Corresponding ROI sizes are $x_{ROI,1} = 21R_c$, $x_{ROI,2} = 91R_c$, and $x_{ROI,3} = 182R_c$ in the case of the smallest, middle, and largest simulation box used, respectively. By implementing the momentum-flux-exchanging *setup 1* (see Figure 1a), where the DPD thermostat acts on all particles within the simulation domain, that is, buffers+ROI, the effect of a frequency on the attenuation and speed of sound is examined.

To check if the temperature profiles are flat and at the expected temperature, we compute them (as discussed in section 3.3) and depict one in Figure 3 (temperature profiles for ultrasound waves with a frequency of $2.76\tau_{DPD}^{-1}$, $2.15\tau_{DPD}^{-1}$, $0.92\tau_{DPD}^{-1}$, $0.46\tau_{DPD}^{-1}$, and $0.27\tau_{DPD}^{-1}$ are shown in Figure S1 in the Supporting Information). Because the temperature profiles are indeed flat, we anticipate that the computed speed of sound
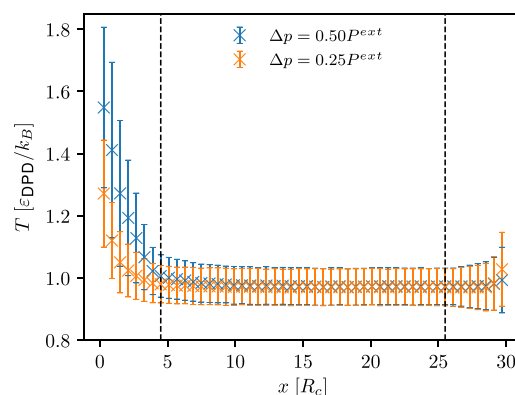

Figure 3. Computed temperature profiles through the simulation box (*setup 1*) for the ultrasound wave with a frequency of $\nu = 1.84\tau_{DPD}^{-1}$ and two different amplitudes. Colored crosses indicate average temperature, while error bars denote the associated standard deviation.

(c_s) will be comparable to the one determined from the EOS of a DPD water (see Table 1). Following the procedure described in section 3.3, we observe a linear increase in the calculated speed of sound with increasing frequency for the low frequency ultrasound waves. However, this is not the case for the high frequency ultrasound waves, since computed values of speed of sound are about the same (see Figure 4). For gases, the speed
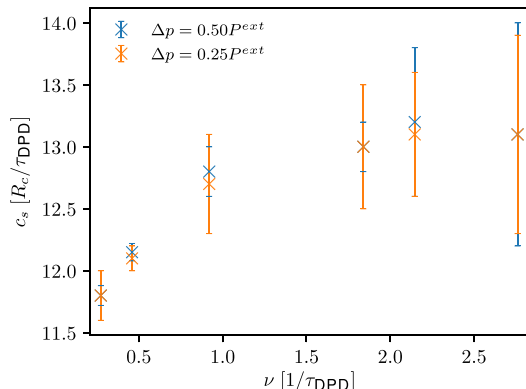

Figure 4. Comparison of the computed speed of sound with associated standard deviations, represented with error bars, for ultrasound waves of different frequencies and two different amplitudes (*setup 1*).

of sound should approach the adiabatic speed of sound for lower frequencies, while for higher frequencies it should approach the isothermal speed of sound.[43] As evident from Figure 4, with decreasing frequency the computed speed of sound is getting closer to the one determined from the EOS of a DPD water (see Table 1) and therefore, ultrasound waves can be considered as isothermal. Using the computed speed of sound, we can calculate the wavelengths of simulated ultrasound waves. The corresponding wavelengths for the ultrasound waves with a frequency of $2.76\tau_{\mathrm{DPD}}^{-1}$, $2.15\tau_{\mathrm{DPD}}^{-1}$, and $1.84\tau_{\mathrm{DPD}}^{-1}$ are $0.25x_{\mathrm{ROI,1}}$, $0.30x_{\mathrm{ROI,1}}$, $0.34x_{\mathrm{ROI,1}}$, respectively, while for the ultrasound waves with a frequency of $0.92\tau_{\mathrm{DPD}}^{-1}$, $0.46\tau_{\mathrm{DPD}}^{-1}$, and $0.27\tau_{\mathrm{DPD}}^{-1}$ they are $0.15x_{\mathrm{ROI,2}}$, $0.15x_{\mathrm{ROI,3}}$, and $0.25x_{\mathrm{ROI,3}}$, respectively.

Interestingly, the attenuation coefficients are observed to increase quadratically with increasing frequency of ultrasound waves (see Figure 5). Similarly, taking propagation of acoustic waves in air, Fletcher[51] also proposed a quadratic increase of attenuation coefficients with increasing frequency.

In addition, as shown in Figure 6, we observe a good agreement of the calculated density signals with the analytical solutions (corresponding to the solution of the wave equation described in section 2.1). Computed density signals for ultrasound waves with a frequency of $2.76\tau_{\mathrm{DPD}}^{-1}$, $2.15\tau_{\mathrm{DPD}}^{-1}$, $0.92\tau_{\mathrm{DPD}}^{-1}$, $0.46\tau_{\mathrm{DPD}}^{-1}$, and $0.27\tau_{\mathrm{DPD}}^{-1}$ are depicted in Figure S5.

Assuming that the friction coefficient $\gamma_\parallel$ affects the propagation of ultrasound waves, its effect is studied by implementing the momentum-flux-exchanging *setup 2*. Accordingly, the value of a friction coefficient through the ROI $\gamma_{\parallel,\mathrm{ROI}}$ is varied between $0.0M_{\mathrm{DPD}}/\tau_{\mathrm{DPD}}$ and $4.0M_{\mathrm{DPD}}/\tau_{\mathrm{DPD}}$, while in the buffer regions it is constant. With this *setup* (see Figure 1b) and simulation box of size $30 \times 10 \times 10R_c^3$ in the x-, y-, and z-directions, only the high frequency ultrasound waves are simulated, since these ultrasound waves are also the most attenuated. Corresponding ROI size is $x_{\mathrm{ROI}} = 21R_c$. As for *setup 1*, we get flat temperature profiles through the ROI at the
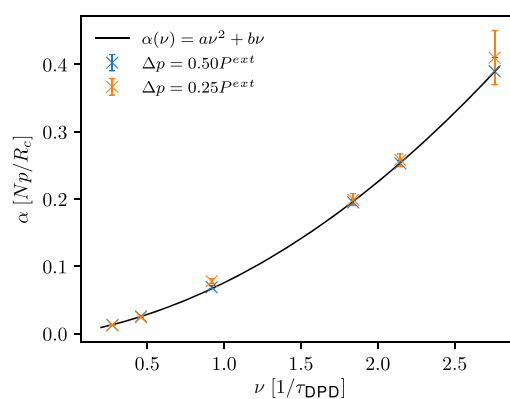

Figure 5. Comparison of the computed attenuation coefficients with associated standard deviations, represented with error bars, for ultrasound waves of different frequencies and two different amplitudes (*setup 1*). Crosses indicate results calculated from simulations using OBMD, while the black line corresponds to the quadratic dependence of the attenuation coefficients on the frequency for ultrasound waves with an amplitude of $0.50P^{\mathrm{ext}}$, where $a = (0.0372 \pm 0.0007)Np\tau_{\mathrm{DPD}}^2/R_c$ and $b = (0.038 \pm 0.001)Np\tau_{\mathrm{DPD}}^2/R_c$.
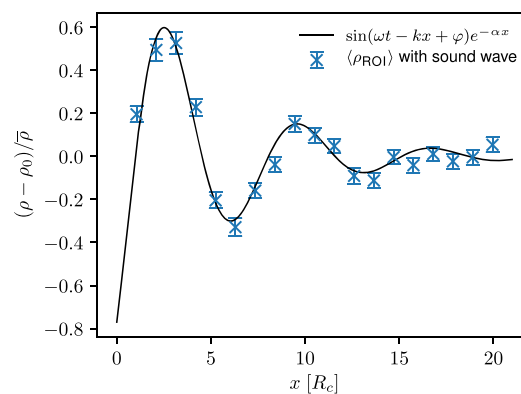

Figure 6. Computed density signal through the ROI for the ultrasound wave with a frequency of $1.84\tau_{\mathrm{DPD}}^{-1}$ and an amplitude of $0.50P^{\mathrm{ext}}$ at time $t = t_0$ (*setup 1*). Blue crosses indicate results calculated from simulation using OBMD, error bars represent the associated standard error, and the black line corresponds to the analytical solution.

expected temperature regardless of the friction coefficient used (see Figure S2).

Although $\gamma_{\parallel,\mathrm{ROI}}$ does not affect the temperature profile, it does affect the computed speed of sound. A slight linear increase of speed of sound with increasing $\gamma_{\parallel,\mathrm{ROI}}$ is indicated (see Figure 7). In contrast to *setup 1*, a different speed of sound is computed for different $\gamma_{\parallel,\mathrm{ROI}}$, which leads to slightly shorter wavelengths of the simulated ultrasound waves. Intriguingly, with decreasing $\gamma_{\parallel,\mathrm{ROI}}$, the computed speed of sound approaches the one determined from the EOS of a DPD water (see Table 1). Accordingly, ultrasound waves are considered as isothermal.

As it turns out, $\gamma_{\parallel,\mathrm{ROI}}$ greatly affects the attenuation of ultrasound waves, as depicted in Figure 8. Attenuation coefficients also appear to increase linearly with increasing $\gamma_{\parallel,\mathrm{ROI}}$ and, as evident from Figure 8, this increase is faster for the ultrasound wave with the highest frequency. To show the influence of the selected $\gamma_{\parallel,\mathrm{ROI}}$ on the propagation of ultrasound waves, calculated density signals through the ROI for the ultrasound wave with a frequency of $1.84\tau_{\mathrm{DPD}}^{-1}$ are
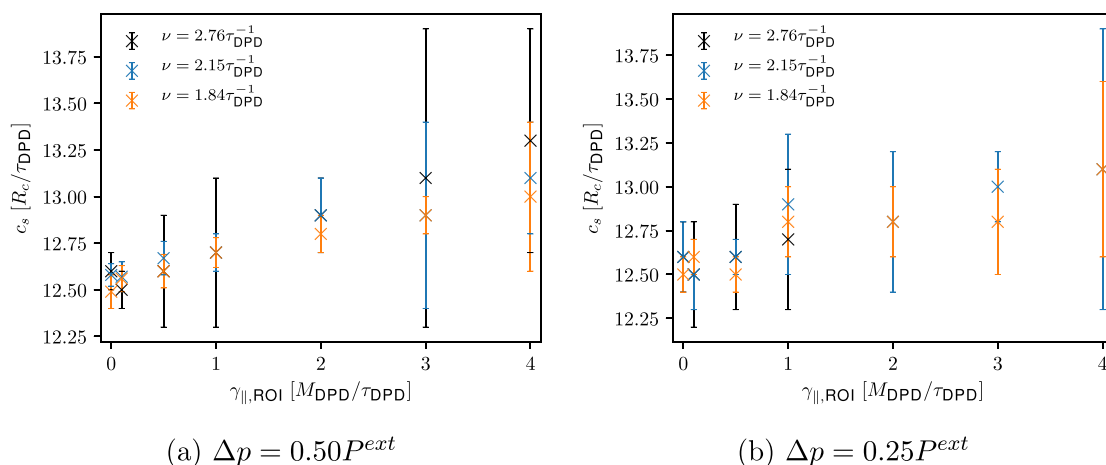
(a) $\Delta p = 0.50 P^{ext}$ (b) $\Delta p = 0.25 P^{ext}$

Figure 7. Comparison of the computed speed of sound with respect to the friction coefficients $\gamma_{\parallel,\text{ROI}}$ used for simulation of ultrasound waves of different frequencies and two different amplitudes (*setup 2*).

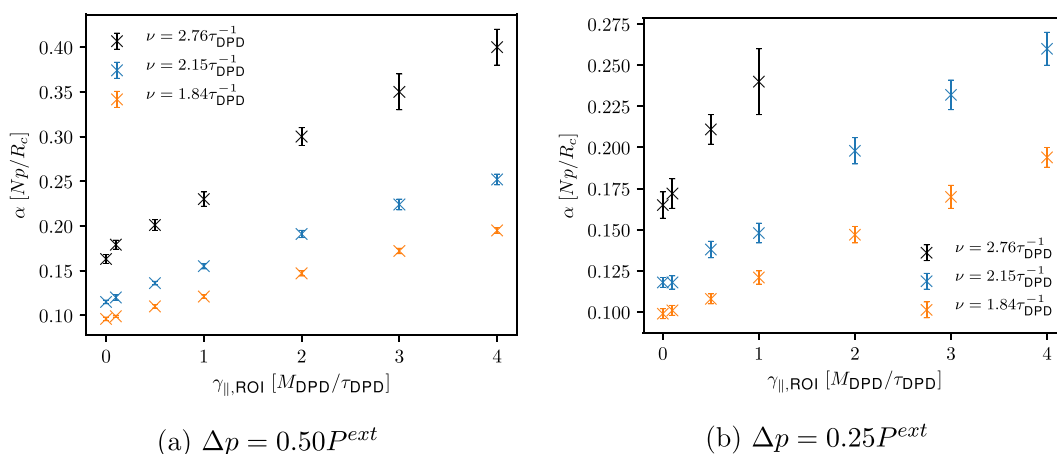(a) $\Delta p = 0.50 P^{ext}$ (b) $\Delta p = 0.25 P^{ext}$

Figure 8. Comparison of the computed attenuation coefficients (*setup 2*).

shown in Figure 9. Similar to *setup 1*, we observe a good agreement between the calculated density signals and the analytical solutions regardless of the friction coefficient $\gamma_{\parallel,\text{ROI}}$ used. Computed density signals for the ultrasound waves with a frequency of $2.76\tau_{\text{DPD}}^{-1}$ and $2.15\tau_{\text{DPD}}^{-1}$ are shown in Figures S6, S7, and S8 in the Supporting Information.

The observed influence of the selected $\gamma_{\parallel,\text{ROI}}$ on the computed properties inspires us to implement the momentum-flux-exchanging *setup 3*, as it allows control of the energy flux without the use of a thermostat. Therefore, the DPD thermostat is completely switched off. We choose the same simulation box size as in *setup 1*, since we simulate ultrasound waves of the same frequencies. Here, we show results for ultrasound waves with an amplitude of $0.25P^{\text{ext}}$, while at higher pressure amplitude the control of the energy transfer contribution (defined by eq 21) is rather challenging. As for *setups 1* and *2*, we observe flat temperature profiles through the ROI at the expected temperature (see Figure S3 in the Supporting Information).

In contrast to the momentum-flux-exchanging *setups 1* and *2*, using the energy-flux-exchanging *setup 3* indicates that the calculated speed of sound does not depend on the frequency of ultrasound waves (see Table 2). As for *setup 2*, we observe slightly shorter wavelengths. Nevertheless, the computed values of speed of sound are close to the one determined from the EOS of a DPD water (see Table 1) and therefore,

ultrasound waves are still considered as isothermal. As expected, we also observe that the attenuation of ultrasound waves with increasing frequency increases. Despite using another approach, we observe a good agreement between the computed density profiles and the analytical solutions, as shown in Figure 10 for the ultrasound wave with a frequency of $1.84\tau_{\text{DPD}}^{-1}$. Calculated density signals for the ultrasound waves with a frequency of $2.76\tau_{\text{DPD}}^{-1}$ and $2.15\tau_{\text{DPD}}^{-1}$ are depicted in Figure S9 in the Supporting Information.

Finally, let us comment on the performance of the *setups 1*, *2*, and *3* for simulations of ultrasound waves in the THz range. To this end, we compare the results where the friction coefficient $\gamma_{\parallel,\text{ROI}} = 0.0 M_{\text{DPD}}/\tau_{\text{DPD}}$ for *setup 2*. We expect that the determined speed of sound for ultrasound waves simulated using *setups 2* and *3* will be comparable. For the ultrasound waves simulated using *setup 1*, we compute the highest values of speed of sound, while the calculated values of speed of sound are within error bars for *setups 2* and *3*, as depicted in Figure 11. Note that as $\gamma_{\parallel,\text{ROI}}$ increases (*setup 2*), the values of speed of sound approach the speed of sound determined for the *setup 1*. This is not surprising, since the momentum-flux-exchanging *setup 2* is another variant of the momentum-flux-exchanging *setup 1*, where for the latter a constant $\gamma_{\parallel}$ is used through the simulation domain (see Table 1).

For the same reason, we anticipate that the computed attenuation coefficients for ultrasound waves simulated using
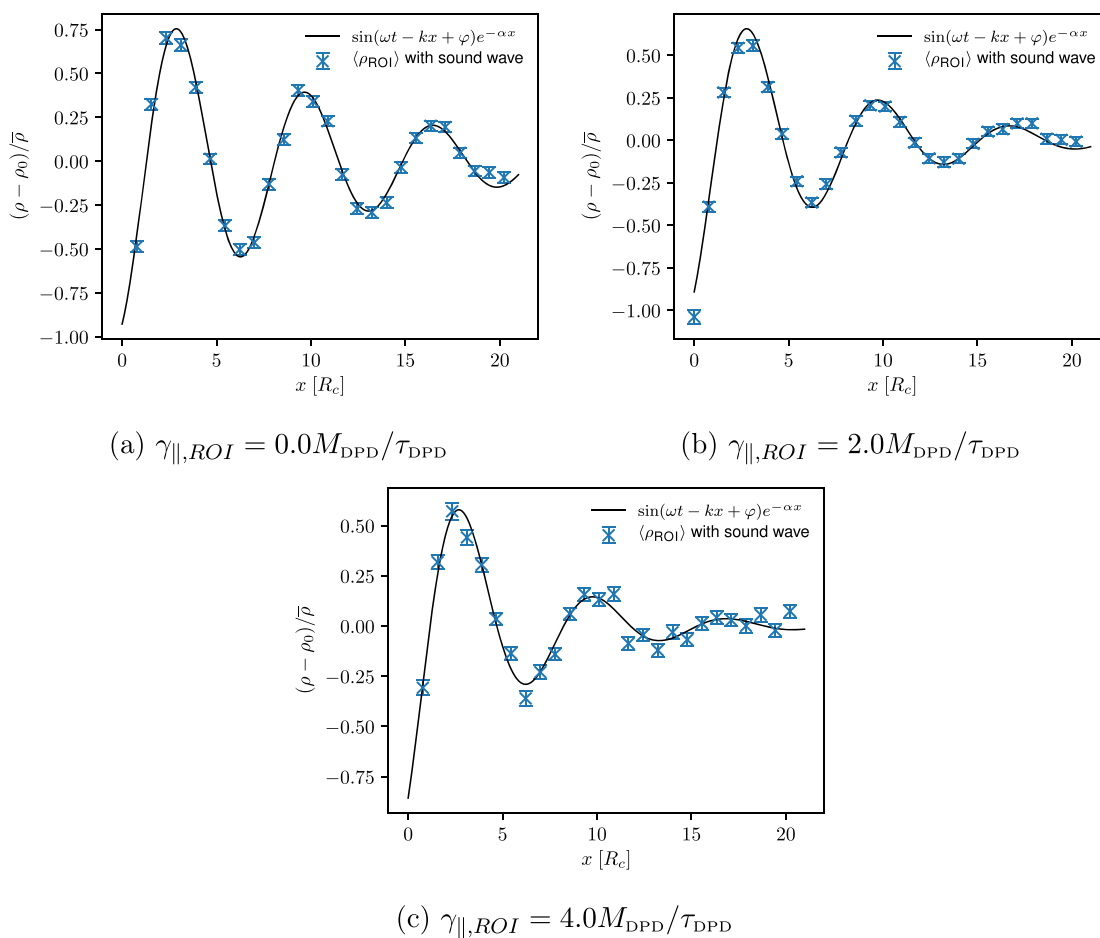
(a) $\gamma_{\parallel,ROI} = 0.0 M_{\mathrm{DPD}}/\tau_{\mathrm{DPD}}$

(b) $\gamma_{\parallel,ROI} = 2.0 M_{\mathrm{DPD}}/\tau_{\mathrm{DPD}}$

(c) $\gamma_{\parallel,ROI} = 4.0 M_{\mathrm{DPD}}/\tau_{\mathrm{DPD}}$

Figure 9. Computed density signals through the ROI for the ultrasound wave with a frequency of $1.84\tau_{\mathrm{DPD}}^{-1}$ and an amplitude of $0.50P^{\mathrm{ext}}$ at time $t = t_0$ and for three different friction coefficients $\gamma_{\parallel,\mathrm{ROI}}$ used (*setup 2*).

Table 2. Computed Speed of Sound and Attenuation Coefficients for Ultrasound Waves of Different Frequencies and an Amplitude of $0.25P^{\mathrm{ext}}$ (*setup 3*)

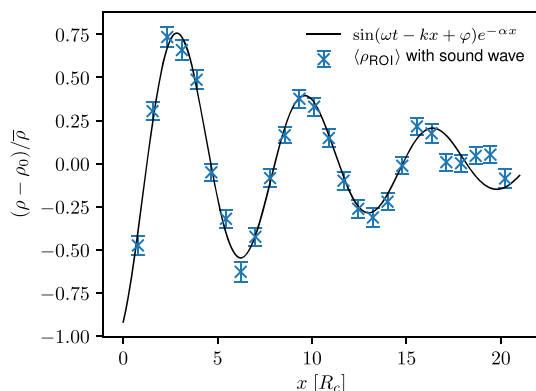| $\nu\,[1/\tau_{\mathrm{DPD}}]$	$c_s\,[R_c/\tau_{\mathrm{DPD}}]$	$\alpha\,[Np/R_c]$
2.76	12.4 ± 0.3	0.158 ± 0.007
2.15	12.4 ± 0.1	0.115 ± 0.003
1.84	12.4 ± 0.1	0.096 ± 0.003

Figure 10. Computed density signal through the ROI for the ultrasound wave with a frequency of $1.84\tau_{\mathrm{DPD}}^{-1}$ and an amplitude of $0.25P^{\mathrm{ext}}$ at time $t = t_0$ (*setup 3*).
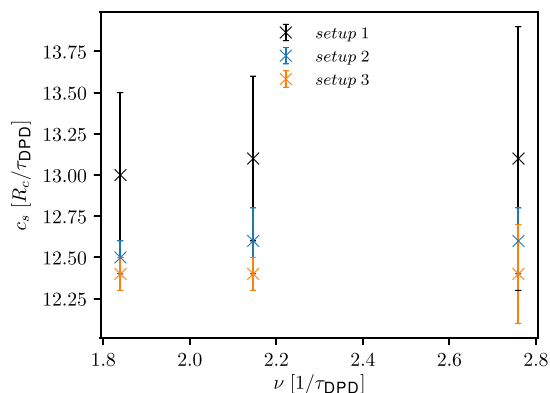

Figure 11. Comparison of the computed speed of sound with respect to the *setups* used for ultrasound waves of different frequencies and an amplitude of $0.25P^{\mathrm{ext}}$.

setups 2 and *3* will also be comparable. As shown in Figure 12, the computed attenuation coefficients are within error bars, while the ultrasound waves simulated employing *setup 1* are the most attenuated. Similar as in the case of the speed of sound, with increasing $\gamma_{\parallel,\mathrm{ROI}}$ (*setup 2*) the attenuation of ultrasound waves increases.

The results in Figure 12 indicate that the attenuation of ultrasound waves can be reduced by using smaller friction coefficients when applying the momentum-flux-exchanging *setup 2* or simply by implementing the energy-flux-exchanging
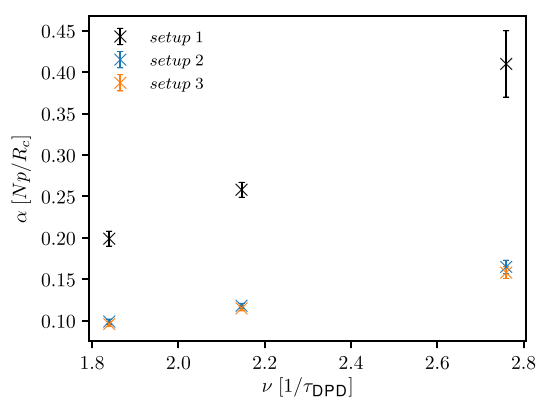
Figure 12. Comparison of the computed attenuation coefficients for different *setups*.

setup 3. For all *setups*, we observe a good agreement between the computed density signals and analytical solutions. However, using different *setups*, one needs to be aware of the influence of the selected friction coefficients (e.g., $\gamma_\parallel$, $\gamma_{\parallel,\mathrm{ROI}}$, and $\gamma_\perp$) and also other parameters on the physical properties (for example, viscosity) of the simulated system.

Because in our future work the presented virtual ultrasound machine will be used to excite the low-frequency vibrational modes of proteins in water, we also test it to propagate ultrasound waves through the atomistic water. For this purpose, we use the momentum-flux-exchanging *setup*, where the DPD thermostat acts on all particles within the simulation domain (i.e., buffers+ROI), combined with AdResS (see Figure 2). We choose to simulate ultrasound waves with a frequency of $0.31\tau_{\mathrm{MD}}^{-1}$ and $0.21\tau_{\mathrm{MD}}^{-1}$, while they belong to the frequency range corresponding to the vibrational modes in proteins. Using a simulation box of size $49.96 \times 8.85 \times 8.85\sigma^3$ in the x-, y-, and z-directions, we simulate ultrasound waves with a frequency of $0.31\tau_{\mathrm{MD}}^{-1}$, and while using a simulation box of size $99.93 \times 8.85 \times 8.85\sigma^3$, we simulate ultrasound waves with a frequency of $0.21\tau_{\mathrm{MD}}^{-1}$. Corresponding ROI sizes are $x_{\mathrm{ROI},1} = 35.40\sigma$ in the case of a smaller simulation box and $x_{\mathrm{ROI},2} = 85.37\sigma$ in the case of a larger simulation box. We simulate ultrasound waves with different pressure amplitudes, but only those with higher amplitude (i.e., $\Delta p = 1.3P^{\mathrm{ext}}$ and $2.0P^{\mathrm{ext}}$) are suitable for our analysis due to very noisy signals obtained for ultrasound waves with lower pressure amplitudes. As for simulations employing the DPD water model and implementing different *setups*, we observe flat temperature profiles through the ROI at the expected temperature (see Figure S4 in the Supporting Information).

To compute the speed of sound, we follow the same procedure as in DPD simulations. We observe that with decreasing frequency, the calculated speed of sound approaches to the one determined from the EOS of the SPC water (see Tables 2 and 1). Therefore, simulated ultrasound waves can be considered as isothermal. Using the computed speed of sound, we calculate the corresponding wavelengths; that is, for the ultrasound wave with a frequency of $0.31\tau_{\mathrm{MD}}^{-1}$ it is approximately $x_{\mathrm{ROI},1}$, while for the ultrasound wave with a frequency of $0.21\tau_{\mathrm{MD}}^{-1}$ it is equal to $0.55x_{\mathrm{ROI},2}$.

As expected, we observe that the high frequency ultrasound wave is more attenuated (see Table 3). Interestingly, even though we matched the viscosity of DPD to the reference value of the atomistic water, nevertheless, slightly higher attenuation coefficients are determined for the atomistic system. Similarly,

Table 3. Computed Speed of Sound and Attenuation Coefficients with Associated Standard Deviations for Ultrasound Waves of Different Frequencies and Two Different Amplitudes (AdResS Simulation)

$\nu[1/\tau_{\mathrm{MD}}]$	Δp	$c_s[\sigma/\tau_{\mathrm{MD}}]$	$\alpha[Np/\sigma]$
0.31	$2.0P^{\mathrm{ext}}$	11.6 ± 1.0	0.080 ± 0.006
	$1.3P^{\mathrm{ext}}$	11.6 ± 1.4	0.081 ± 0.006
0.21	$2.0P^{\mathrm{ext}}$	10.6 ± 0.8	0.054 ± 0.001
	$1.3P^{\mathrm{ext}}$	9.9 ± 0.8	0.047 ± 0.003

this applies also to the computed speed of sound. We attribute this disagreement to softer interactions between DPD waters in comparison to atomistic water. As for DPD simulations, computed density signals are in a good agreement with the analytical solutions (see Figure S10 in the Supporting Information).

The presented virtual ultrasound machine will allow us to study different physical phenomena occurring during the ultrasound propagation.

5. CONCLUSIONS AND OUTLOOK

In this work, we developed the particle-based virtual ultrasound machine and tested it in simulations of ultrasound waves in the THz range using DPD and atomistic water models. The results of our particle-based ultrasound simulations show that our approach is capable of reproducing the fluctuating hydrodynamics description of ultrasound in the continuum limit. At high frequencies, sound waves in gases can be considered as adiabatic, whereas at low frequencies they can be considered as isothermal. If the frequency of a sound wave ω is comparable to the frequency associated with the thermal conduction of a medium ω_{TC}, as in water, then it is not clear a priori which approximation works better. To clarify this issue, the DPD water model was used and momentum-flux-exchanging and energy-exchanging schemes were implemented and tested. Our results indicate that the isothermal classification is more appropriate. We also studied the effect of thermostat parameters on the attenuation of ultrasound waves and computed speed of sound. The greatest attenuation of ultrasound waves was observed for the momentum-flux-exchanging scheme, in which DPD and TDPD thermostats acted on all particles within simulation domain (i.e., buffer +ROI). For this scheme, we also observed a linear increase in the computed speed of sound for lower frequency ultrasound waves. Furthermore, the computed speed of sound slightly depends on the friction coefficients $\gamma_{\parallel,\mathrm{ROI}}$.

To conclude, the developed method enables us to study different physical phenomena associated with ultrasound-soft(bio) matter interactions. In our future work, we aim to employ the presented virtual ultrasound machine to study the low-frequency vibrational modes of biomolecules in water. Moreover, we will perform simulations of adiabatic ultrasound waves propagating in water (i.e., simulations of ultrasound waves at lower frequencies, i.e., in the GHz−MHz range, that can penetrate centimeters deep). Accordingly, larger systems will be employed and the energy-flux-exchanging approach will be implemented.

■ ASSOCIATED CONTENT

ⓈⒾ Supporting Information

The Supporting Information is available free of charge at https://pubs.acs.org/doi/10.1021/acs.jctc.1c01020.

Computed temperature profiles and density signals for ultrasound waves of different frequencies and amplitudes simulated by OBMD (PDF)

AUTHOR INFORMATION

Corresponding Author

Matej Praprotnik − *Laboratory for Molecular Modeling, National Institute of Chemistry, Ljubljana SI-1001, Slovenia; Department of Physics, Faculty of Mathematics and Physics, University of Ljubljana, Ljubljana SI-1000, Slovenia;* ⓞ orcid.org/0000-0003-0825-1659; Email: praprot@cmm.ki.si

Author

Petra Papež − *Laboratory for Molecular Modeling, National Institute of Chemistry, Ljubljana SI-1001, Slovenia; Department of Physics, Faculty of Mathematics and Physics, University of Ljubljana, Ljubljana SI-1000, Slovenia*

Complete contact information is available at:
https://pubs.acs.org/10.1021/acs.jctc.1c01020

Notes

The authors declare no competing financial interest.

REFERENCES

(1) Udroiu, I. Ultrasonic drug delivery in Oncology. *JBUON* **2015**, *20*, 381−390.

(2) Maresca, D.; Sawyer, D. P.; Renaud, G.; Lee-Gosselin, A.; Shapiro, M. G. Nonlinear X-Wave Ultrasound Imaging of Acoustic Biomolecules. *Phys. Rev. X* **2018**, *8*, No. 041002.

(3) Maresca, D.; Lakshmanan, A.; Abedi, M.; Bar-Zion, A.; Farhadi, A.; Lu, G. J.; Szablowski, J. O.; Wu, D.; Yoo, S.; Shapiro, M. G. Biomolecular Ultrasound and Sonogenetics. *Annu. Rev. Chem. Biomol. Eng.* **2018**, *9*, 229−252.

(4) Sofferman, R. A. In *Ultrasound of the Thyroid and Parathyroid Glands*; Sofferman, R. A., Ahuja, A. T., Eds.; Springer: New York, NY, 2012; pp 9−19.

(5) Maresca, D.; Lakshmanan, A.; Lee-Gosselin, A.; Melis, J. M.; Ni, Y.-L.; Bourdeau, R. W.; Kochmann, D. M.; Shapiro, M. G. Nonlinear ultrasound imaging of nanoscale acoustic biomolecules. *Appl. Phys. Lett.* **2017**, *110*, No. 073704.

(6) Léveque, J.-M.; Cravotto, G.; Delattre, F.; Cintas, P. *Organic Sonochemistry: Challenges and Perspectives for the 21st Century*; Ultrasound and Sonochemistry; Springer International Publishing, 2018.

(7) Ashokkumar, M., Ed. *Handbook of Ultrasonics and Sonochemistry*; Springer: Singapore, 2016.

(8) Lempriere, B. M. *Ultrasound and Elastic Waves: Frequently Asked Questions*; Elsevier, 2003.

(9) Faisal, N. H.; Ahmed, R.; Reuben, R. L. Indentation testing and its acoustic emission response: applications and emerging trends. *Int. Mater. Rev.* **2011**, *56*, 98−142.

(10) Lee, H.; Kim, H.; Han, H.; Lee, M.; Lee, S.; Yoo, H.; Chang, J. H.; Kim, H. Microbubbles used for contrast enhanced ultrasound and theragnosis: a review of principles to applications. *Biomed. Eng. Lett.* **2017**, *7*, 59−69.

(11) Lindner, J. R. Microbubbles in medical imaging: current applications and future directions. *Nat. Rev. Drug Discovery* **2004**, *3*, 527−533.

(12) Cosgrove, D. Ultrasound Contrast Agents: An Overview. *Eur. J. Radiol.* **2006**, *60*, 324−330.

(13) Deshpande, N.; Needles, A.; Willmann, J. K. Molecular ultrasound imaging: current ctatus and future directions. *Clin. Radiol.* **2010**, *65*, 567−581.

(14) Izadifar, Z.; Babyn, P.; Chapman, D. Mechanical and Biological Effects of Ultrasound: A Review of Present Knowledge. *Ultrasound Med. Biol.* **2017**, *43*, 1085−1104.

(15) Macé, E.; Montaldo, G.; Cohen, I.; Baulac, M.; Fink, M.; Tanter, M. Functional ultrasound imaging of the brain. *Nat. Methods* **2011**, *8*, 662−664.

(16) Rayleigh, J. W. S. *The Theory of Sound*; Dover Publication: New York, 1945.

(17) Goodman, J. W. *Introduction to Fourier Optics*, 2nd ed.; McGraw-Hill: New York, 1945.

(18) Vyas, U.; Christensen, D. Ultrasound beam propagation using the hybrid angular spectrum method. 30th Annual International Conference of the IEEE Engineering in Medicine and Biology Society, Vancouver, BC, Canada, April 7, 2008, pp 2526−2529.

(19) Zemp, R. J.; Tavakkoli, J.; Cobbold, R. S. C. Modeling of nonlinear ultrasound propagation in tissue from array transducers. *J. Acoust. Soc. Am.* **2003**, *113*, 139−152.

(20) Schwenke, M.; Georgii, J.; Preusser, T. Fast Numerical Simulation of Focused Ultrasound Treatments During Respiratory Motion With Discontinuous Motion Boundaries. *IEEE Trans. Biomed. Eng.* **2017**, *64*, 1455−1468.

(21) Zeng, X.; McGough, R. J. Optimal simulations of ultrasonic fields produced by large thermal therapy arrays using the angular spectrum approach. *J. Acoust. Soc. Am.* **2009**, *125*, 2967−2977.

(22) Wu, P.; Stepinski, T. Extension of the angular spectrum approach to curved radiators. *J. Acoust. Soc. Am.* **1999**, *105*, 2618−2627.

(23) Wu, P.; Kazys, R.; Stepinski, T. Optimal selection of parameters for the angular spectrum approach to numerically evaluate acoustic fields. *J. Acoust. Soc. Am.* **1997**, *101*, 125−134.

(24) Bahvalov, N. S.; Žilejkin, J. M.; Zabolotskaja, E. A. *Nonlinear theory of sound beams*; American Institute of Physics: New York, 1987.

(25) Ginter, S.; Liebler, M.; Steiger, E.; Dreyer, T.; Riedlinger, R. E. Full-wave modeling of therapeutic ultrasound: Nonlinear ultrasound propagation in ideal fluids. *J. Acoust. Soc. Am.* **2002**, *111*, 2049−2059.

(26) Tavakkoli, J.; Cathignol, D.; Souchon, R.; Sapozhnikov, O. A. Modeling of pulsed finite-amplitude focused sound beams in time domain. *J. Acoust. Soc. Am.* **1998**, *104*, 2061−2072.

(27) Kythe, P. K. *An Introduction to Boundary Element Methods*; CRC Press, 1995.

(28) Ihlenburg, F. *Finite Element Analysis of Acoustic Scatterings*; Springer: New York, 1998.

(29) Harari, I. A survey of finite element methods for time-harmonic acoustics. *Comput. Methods Appl. Mech. Eng.* **2006**, *195*, 1594−1607.

(30) Warszawski, A.; Soares, D.; Mansur, W. J. A FEM−BEM coupling procedure to model the propagation of interacting acoustic−acoustic/acoustic−elastic waves through axisymmetric media. *Comput. Methods Appl. Mech. Eng.* **2008**, *197*, 3828−3835.

(31) Feng, J.; Zheng, X.; Wang, H.; Wang, H.; Zou, Y.; Liu, Y.; Yao, Z. Low-Frequency Acoustic-Structure Analysis Using Coupled FEM-BEM Method. *Math. Probl. Eng.* **2013**, *2013*, No. e583079.

(32) Tadeu, A.; Castro, I. Coupling the BEM/TBEM and the MFS for the Numerical Simulation of Wave Propagation in Heterogeneous Fluid-Solid Media. *Math. Probl. Eng.* **2011**, *2011*, No. e159389.

(33) Uras, R. A.; Chang, C.-T.; Chen, Y.; Liu, W. K. Multiresolution Reproducing Kernel Particle Methods in Acoustics. *J. Comp. Acous.* **1997**, *05*, 71−94.

(34) Bouillard, P.; Suleaub, S. Element-Free Galerkin solutions for Helmholtz problems: fomulation and numerical assessment of the pollution effect. *Comput. Methods Appl. Mech. Eng.* **1998**, *162*, 317−335.

Journal of Chemical Theory and Computation
    pubs.acs.org/JCTC
    Article

(35) Zhang, Y.; Zhang, T.; Ouyang, H.; Li, T. Y. SPH simulation of sound propagation and interference. ICCM2014, Cambridge, England, July 28-30, 2014, 2830.

(36) Zhang, Y.; Zhang, T.; Ouyang, H.; Li, T. Y. SPH Simulation of Acoustic Waves: Effects of Frequency, Sound Pressure, and Particle Spacing. *Math. Probl. Eng.* **2015**, *2015*, No. e348314.

(37) Koumoutsakos, P. Multiscale flow simulations using particles. *Annu. Rev. Fluid Mech.* **2005**, *37*, 457−487.

(38) De Fabritiis, G.; Delgado-Buscalioni, R.; Coveney, P. V. Multiscale Modeling of Liquids with Molecular Specificity. *Phys. Rev. Lett.* **2006**, *97*, 134501.

(39) Delgado-Buscalioni, R.; De Fabritiis, G. Embedding molecular dynamics within fluctuating hydrodynamics in multiscale simulations of liquids. *Phys. Rev. E* **2007**, *76*, No. 036709.

(40) Korotkin, I.; Karabasov, S.; Nerukh, D.; Markesteijn, A.; Scukins, A.; Farafonov, V.; Pavlov, E. A hybrid molecular dynamics/fluctuating hydrodynamics method for modelling liquids at multiple scales in space and time. *J. Chem. Phys.* **2015**, *143*, No. 014110.

(41) Hu, J.; Korotkin, I. A.; Karabasov, S. A. A multi-resolution particle/fluctuating hydrodynamics model for hybrid simulations of liquids based on the two-phase flow analogy. *J. Chem. Phys.* **2018**, *149*, No. 084108.

(42) Korotkin, I. A.; Karabasov, S. A. A generalised Landau-Lifshitz fluctuating hydrodynamics model for concurrent simulations of liquids at atomistic and continuum resolution. *J. Chem. Phys.* **2018**, *149*, 244101.

(43) Wu, J. Are sound waves isothermal or adiabatic? *Am. J. Phys.* **1990**, *58*, 694−696.

(44) Pierce, A. D. *Acoustics: An Introduction to Its Physical Principles and Applications*; Springer International Publishing, 2019.

(45) Berendsen, H. J.; Postma, J. P.; van Gunsteren, W. F.; Hermans, J. In *Intermolecular Forces*; Pullman, B., Ed.; Reidel: Dordrecht, 1981; pp 331−342.

(46) Landau, L. D.; Lifshitz, E. M.*Fluid mechanics: Vol. 6 of Course of theoretical physics*; Elsevier, 2009.

(47) Chowdhury, S. M.; Lee, T.; Willmann, J. K. Ultrasound-guided drug delivery in cancer. *Ultrasonography* **2017**, *36*, 171−184.

(48) Lentacker, I.; De Cock, I.; Deckers, R.; De Smedt, S. C.; Moonen, C. T. W. Understanding ultrasound induced sonoporation: Definitions and underlying mechanisms. *Adv. Drug Delivery Rev.* **2014**, *72*, 49−64.

(49) Pitt, W. G.; Husseini, G. A.; Staples, B. J. Ultrasonic drug delivery − a general review. *Expert Opin. Drug Delivery* **2004**, *1*, 37−56.

(50) Wang, T.-Y.; Wilson, K. E.; Machtaler, S.; Willmann, J. K. Ultrasound and microbubble guided drug delivery: mechanistic understanding and clinical implications. *Curr. Pharm. Biotechnol.* **2014**, *14*, 743−752.

(51) Fletcher, N. H. Adiabatic Assumption for Wave Propagation. *Am. J. Phys.* **1974**, *42*, 487−489.

(52) Español, P. Hydrodynamics from dissipative particle dynamics. *Phys. Rev. E* **1995**, *52*, 1734−1742.

(53) Marsh, C. A.; Backx, G.; Ernst, M. H. Static and dynamic properties of dissipative particle dynamics. *Phys. Rev. E* **1997**, *56*, 1676−1691.

(54) Li, Z.; Bian, X.; Li, X.; Deng, M.; Tang, Y.-H.; Caswell, B.; Karniadakis, G. E.*Particles in Flows*; Springer, 2017; pp 255−326.

(55) Nikolić, D.; Moffat, K. A.; Farrugia, V. M.; Kobryn, A. E.; Gusarov, S.; Wosnick, J. H.; Kovalenko, A. Multi-scale modeling and synthesis of polyester ionomers. *Phys. Chem. Chem. Phys.* **2013**, *15*, 6128−6138.

(56) Hafskjold, B.; Liew, C. C.; Shinoda, W. Can Such Long Time Steps Really Be Used in Dissipative Particle Dynamics Simulations? *Mol. Simul.* **2004**, *30*, 879−885.

(57) Boromand, A.; Jamali, S.; Maia, J. M. Viscosity measurement techniques in Dissipative Particle Dynamics. *Comput. Phys. Commun.* **2015**, *196*, 149−160.

(58) Venturoli, M.; Smit, B. Simulating the self-assembly of model membranes. *PhysChemComm.* **1999**, *2*, 45−49.

(59) Grafmüller, A.; Shillcock, J.; Lipowsky, R. The Fusion of Membranes and Vesicles: Pathway and Energy Barriers from Dissipative Particle Dynamics. *Biophys. J.* **2009**, *96*, 2658−2675.

(60) Groot, R. D.; Rabone, K. L. Mesoscopic Simulation of Cell Membrane Damage, Morphology Change and Rupture by Nonionic Surfactants. *Biophys. J.* **2001**, *81*, 725−736.

(61) Yamamoto, S.; Maruyama, Y.; Hyodo, S.-a. Dissipative particle dynamics study of spontaneous vesicle formation of amphiphilic molecules. *J. Chem. Phys.* **2002**, *116*, 5842−5849.

(62) Groot, R. D.; Warren, P. B. Dissipative particle dynamics: Bridging the gap between atomistic and mesoscopic simulation. *J. Chem. Phys.* **1997**, *107*, 4423−4435.

(63) Español, P.; Warren, P. Statistical Mechanics of Dissipative Particle Dynamics. *EPL* **1995**, *30*, 191−196.

(64) Soddemann, T.; Dünweg, B.; Kremer, K. Dissipative particle dynamics: A useful thermostat for equilibrium and nonequilibrium molecular dynamics simulations. *Phys. Rev. E* **2003**, *68*, No. 046702.

(65) Junghans, C.; Praprotnik, M.; Kremer, K. Transport properties controlled by a thermostat: An extended dissipative particle dynamics thermostat. *Soft Matter* **2008**, *4*, 156−161.

(66) Flekkøy, E. G.; Delgado-Buscalioni, R.; Coveney, P. V. Flux boundary conditions in particle simulations. *Phys. Rev. E* **2005**, *72*, No. 026703.

(67) Delgado-Buscalioni, R. Tools for Multiscale Simulation of Liquids Using Open Molecular Dynamics. *Numerical Analysis of Multiscale Computations*; Lecture Notes in Computer Science Engineering; Springer Verlag: Berlin, Heidelberg, 2012; pp 145−166.

(68) Delgado-Buscalioni, R.; Sablić, J.; Praprotnik, M. Open boundary molecular dynamics. *Eur. Phys. J. Spec. Top.* **2015**, *224*, 2331−2349.

(69) Sablić, J.; Praprotnik, M.; Delgado-Buscalioni, R. Open boundary molecular dynamics of sheared star-polymer melts. *Soft Matter* **2016**, *12*, 2416−2439.

(70) Zavadlav, J.; Sablić, J.; Podgornik, R.; Praprotnik, M. Open-Boundary Molecular Dynamics of a DNA Molecule in a Hybrid Explicit/Implicit Salt Solution. *Biophys. J.* **2018**, *114*, 2352−2362.

(71) Delgado-Buscalioni, R.; Coveney, P. V. USHER: An algorithm for particle Insertion in dense fluids. *J. Chem. Phys.* **2003**, *119*, 978−987.

(72) de Fabritiis, G.; Delgado-Buscalioni, R.; Coveney, P. V. Energy controlled insertion of polar molecules in dense fluids. *J. Chem. Phys.* **2004**, *121*, 12139−12142.

(73) De Fabritiis, G.; Serrano, M.; Delgado-Buscalioni, R.; Coveney, P. V. Fluctuating hydrodynamic modeling of fluids at the nanoscale. *Phys. Rev. E* **2007**, *75*, No. 026307.

(74) Delgado-Buscalioni, R.; Coveney, P. V. Continuum-particle hybrid coupling for mass, momentum, and energy transfers in unsteady fluid flow. *Phys. Rev. E* **2003**, *67*, No. 046704.

(75) Delle Site, L.; Praprotnik, M. Molecular systems with open boundaries: Theory and simulation. *Phys. Rep.* **2017**, *693*, 1−56.

(76) Delgado-Buscalioni, R.; Kremer, K.; Praprotnik, M. Concurrent triple-scale simulation of molecular liquids. *J. Chem. Phys.* **2008**, *128*, 114110.

(77) Delgado-Buscalioni, R.; Kremer, K.; Praprotnik, M. Coupling atomistic and continuum hydrodynamics through a mesoscopic model: Application to liquid water. *J. Chem. Phys.* **2009**, *131*, 244107.

(78) Reith, D.; Pütz, M.; Müller-Plathe, F. Deriving effective mesoscale potentials from atomistic simulations. *J. Comput. Chem.* **2003**, *24*, 1624−1636.

(79) Bevc, S.; Junghans, C.; Praprotnik, M. STOCK: Structure mapper and online coarse-graining kit for molecular simulations. *J. Comput. Chem.* **2015**, *36*, 467−477.

(80) Praprotnik, M.; Delle Site, L.; Kremer, K. Adaptive resolution molecular-dynamics simulation: Changing the degrees of freedom on the fly. *J. Chem. Phys.* **2005**, *123*, 224106.

(81) Praprotnik, M.; Delle Site, L.; Kremer, K. Multiscale Simulation of Soft Matter: From Scale Bridging to Adaptive Resolution. *Annu. Rev. Phys. Chem.* **2008**, *59*, 545−571.

(82) Cortes-Huerto, R.; Praprotnik, M.; Kremer, K.; Delle Site, L. From adaptive resolution to molecular dynamics of open systems. *Eur. Phys. J. B* **2021**, *94*, 189.

(83) Praprotnik, M.; Delle Site, L. Multiscale molecular modeling. *Biomolecular Simulations: Methods and Protocols*. Humana Press: Totowa, NJ, 2013; pp 567−583.

(84) Zavadlav, J.; Praprotnik, M. Adaptive resolution simulations coupling atomistic water to dissipative particle dynamics. *J. Chem. Phys.* **2017**, *147*, 114110.

(85) Kumar, A.; Asako, Y.; Abu-Nada, E.; Krafczyk, M.; Faghri, M. From dissipative particle dynamics scales to physical scales: a coarse-graining study for water flow in microchannel. *Microfluid. Nanofluidics* **2009**, *7*, 467−477.

(86) Mark, P.; Nilsson, L. Structure and Dynamics of the TIP3P, SPC, and SPC/E Water Models at 298 K. *J. Phys. Chem. A* **2001**, *105*, 9954−9960.

(87) Fuhrmans, M.; Sanders, B. P.; Marrink, S.-J.; de Vries, A. H. Effects of Bundling on the Properties of the SPC Water Model. *Theor. Chem. Acc.* **2010**, *125*, 335−344.

(88) Zavadlav, J.; Melo, M. N.; Cunha, A. V.; de Vries, A. H.; Marrink, S. J.; Praprotnik, M. Adaptive resolution simulation of MARTINI solvents. *J. Chem. Theory Comput.* **2014**, *10*, 2591−2598.

(89) Zavadlav, J.; Melo, M. N.; Marrink, S. J.; Praprotnik, M. Adaptive resolution simulation of an atomistic protein in MARTINI water. *J. Chem. Phys.* **2014**, *140*, No. 054114.

(90) Miyamoto, S.; Kollman, P. A. Settle: An analytical version of the SHAKE and RATTLE algorithm for rigid water models. *J. Comput. Chem.* **1992**, *13*, 952−962.

(91) Allen, M. P.; Tildesley, D. J.*Computer simulation of liquids*; Clarendon Press, 1987.

(92) Delgado-Buscalioni, R.; Dejoan, A. Nonreflecting boundaries for ultrasound in fluctuating hydrodynamics of open systems. *Phys. Rev. E* **2008**, *78*, No. 046708.

(93) Cowan, M.; Rudnick, J.; Barmatz, M. Effects of random motions on critical point measurements: Liquid-gas systems in microgravity. *Phys. Rev. E* **1996**, *53*, 4490−4501.

(94) Praprotnik, M.; JaneŽič, D. Molecular Dynamics Integration Meets Standard Theory of Molecular Vibrations. *J. Chem. Inf. Model* **2005**, *45*, 1571−1579.

(95) Chou, K. C. Identification of low-frequency modes in protein molecules. *Biochem. J.* **1983**, *215*, 465−469.

(96) Chou, K. C. Low-frequency motions in protein molecules. Beta-sheet and beta-barrel. *Biophys. J.* **1985**, *48*, 289−297.

(97) Balog, E.; Perahia, D.; Smith, J. C.; Merzel, F. Vibrational Softening of a Protein on Ligand Binding. *J. Phys. Chem. B* **2011**, *115*, 6811−6817.

(98) Smith, P. E.; van Gunsteren, W. F. The viscosity of SPC and SPC/E water at 277 and 300 K. *Chem. Phys. Lett.* **1993**, *215*, 315−318.

(99) Song, Y.; Dai, L. L. The shear viscosities of common water models by non-equilibrium molecular dynamics simulations. *Mol. Simul.* **2010**, *36*, 560−567.

(100) Haynes, W. M.; Lide, D. R.; Bruno, T. J. *CRC Handbook of Chemistry and Physics*, 97th ed. CRC, 2016−2017.